HEFAT2012
9th International Conference on Heat Transfer, Fluid Mechanics and Thermodynamics
16 – 18 July 2012
Malta

IN-FLIGHT ICING PREDICTION WITH HIGH SPEED FLOW EFFECTS

Özgen S.* and Canıbek M.†

*Author for correspondence
Department of Aerospace Engineering,
Middle East Technical University,
Ankara, 06800,
Turkey,
E-mail: sozgen@ae.metu.edu.tr

† Flight Sciences Department,
Integrated Aircraft Systems Group,
Turkish Aerospace Industries,
Ankara, 06980,
Turkey,
E-mail: mcanibek@tai.com.tr

ABSTRACT

In the current study, continued efforts to improve a computational in-flight icing prediction tool are introduced. The method involves flow-field calculation around an airfoil using the Hess-Smith panel method, droplet trajectory determination and calculation of droplet collection efficiencies. Next step is to compute convective heat transfer coefficient distribution over the geometry. Computation of the ice accretion rates by establishing a thermodynamical balance and utilization of the Extended Messinger Method forms the focus of the developed computational tool. Finally, integration of ice accretion rates over time yields the ice shapes and the final geometry. Compressibility is accounted for in the droplet trajectory calculations and the thermodynamical model. Three test cases corresponding to different levels of compressibility have been studied and the results have been compared with numerical and experimental data available in the literature. The results show that compressibility is a prominent effect and influences both the ice mass and the extent of the iced region in the predictions.

NOMENCLATURE

Symbol	*Definition*	*Value and/or unit*
a_∞	Speed of sound	m/s
A_p	Droplet cross-sectional area	m^2
B	Ice layer thickness	m
c	Chord length of the airfoil	m
C_D	Droplet drag coefficient	
C_p	Specific heat of air	1006 J/kg.K
C_{pi}	Specific heat of ice	2050 J/kg.K
C_{pw}	Specific heat of water	4218 J/kg.K
D	Droplet drag force	N
d_p	Droplet diameter	m
g	Gravitational acceleration	9.81 m/s^2
h	Water layer thickness	m
k_i	Thermal conductivity of ice	2.18 W/m.K
k_w	Thermal conductivity of water	0.571 W/m.K
L_F	Latent heat of solidification	$3.344x10^5$ J/kg
M	Mach number, $M=V_\infty/a_\infty$	
m	Droplet mass	kg
$\dot{m}_{in}$	Runback water entering the control volume	kg/m^2s
$\dot{m}_e$	Mass lost by evaporation	kg/m^2s
$\dot{m}_s$	Mass lost by sublimation	kg/m^2s
Pr	Laminar Prandtl number of air	0.72
Pr_t	Turbulent Prandtl number of air	0.9
Q_x	Energy terms	
r	Recovery factor, $r=Pr^{1/2}$ for laminar, $r=Pr^{1/3}$ for turbulent flow	
Re	Reynolds number, $Re=\rho V_{rel} d_p/\mu$	
T	Temperature in te ice layer	K
T_a	Ambient temperature	K
T_f	Freezing temperature	K
T_s	Surface temperature of substrate	
t	Time	s
U_e	Local flow velocity outside the boundary layer	m/s
V_∞	Freestream velocity	m/s
V_x, V_y	Flow velocity components at the droplet location	m/s
V_{rel}	Relative velocity	m/s
x, y	Cartesian coordinates	m
$\dot{x}_p, \dot{y}_p$	Droplet velocity components	m/s
$\ddot{x}_p, \ddot{y}_p$	Droplet acceleration components	m/s^2

Special Characters

β	Droplet collection efficiency	
γ_1, γ_2	Angles between the droplet and flow velocity components	radians
μ	Kinematic viscosity of ambient air	Pa.s*
ρ	Ambient density	kg/m^{3*}
ρ_a	Liquid water content	kg/m^3
ρ_i	Density of ice	kg/m^3

ρ_r	Density of rime ice	880 kg/m^3
ρ_g	Density of glaze ice	917 kg/m^3
ρ_w	Density of water	999 kg/m^3
σ_r	Stefan-Boltzmann constant	5.6704x10^{-8}
σ_w	Surface tension of water	0.072 N/m*
θ	Temperature in the water layer	K

* Temperature dependence is accounted for.

PROBLEM FORMULATION AND SOLUTION METHOD

Flowfield Solution

In order to determine the flow velocities required for droplet trajectory calculations, 2-D Hess-Smith panel method is used. The solution also provides the external velocity distribution around the wing section required for boundary layer calculations yielding the convective heat transfer coefficients. The velocities are corrected for compressibility effects using the Prandtl-Glauert compressibility correction:

$$\hat{u} = \bar{u} \Big/ \sqrt{1-M^2}, \quad \hat{v} = \bar{v} \Big/ \sqrt{1-M^2}, \tag{1}$$

where $\bar{u}$ and $\bar{v}$ are the perturbation velocity components in the potential flow due to the presence of the airfoil in incompressible flow and $\hat{u}$ and $\hat{v}$ are the same quantities corrected for compressibility effects.

Droplet Trajectories and Collection Efficiencies

The following assumptions are employed for droplet trajectory computations:

- Droplets are assumed to be spherical,
- The droplets do not affect the flow field,
- Gravity and aerodynamic drag are the only forces acting on the droplets.

The droplet trajectories are computed by the following equations:

$$m\ddot{x}_p = -D\cos\gamma_1, \tag{2}$$

$$m\ddot{y}_p = -D\cos\gamma_2 + mg, \tag{3}$$

with:

$$\gamma_1 = \tan^{-1}\frac{\dot{x}_p - V_x}{V_{rel}}, \quad \gamma_2 = \tan^{-1}\frac{\dot{y}_p - V_y}{V_{rel}}, \tag{4}$$

$$D = \tfrac{1}{2}\rho\, V_{rel}^2 C_D A_p, \tag{5}$$

$$V_{rel} = \sqrt{(\dot{x}_p - V_x)^2 + (\dot{y}_p - V_y)^2}. \tag{6}$$

Droplet drag coefficients are calculated using an empirical drag law based on the droplet Reynolds number [1].

Trajectory calculations start from an upstream location far away from the wing section so that air flow velocity components are sufficiently close to their freestream values. The initial droplet velocity is taken to be the terminal velocity.

The droplet trajectories are obtained by integrating equations (2-3) over time until the droplet impacts the geometry. The droplet impact pattern on the section determines the amount of water that impinges on the surface, the impingement region and the droplet collection efficiency distribution, $\beta(x,y)$. Figure 1 shows the droplet trajectories and Figure 2 shows the resulting collection efficiency distribution for Case 40, see below. The collection efficiency has a maximum near the stagnation point and rapidly diminishes in the downstream direction both for the upper and lower surfaces of the airfoil.

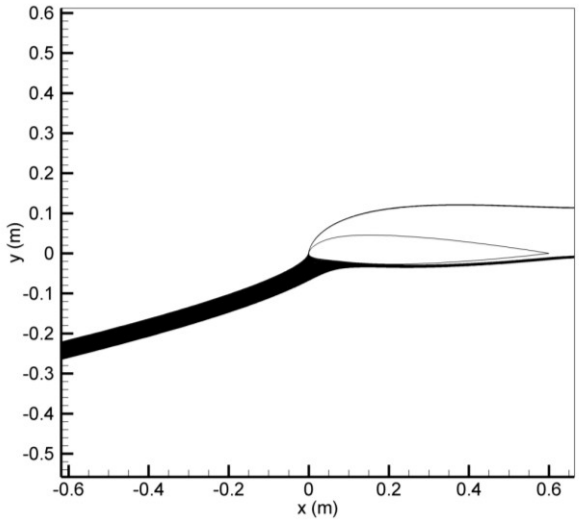

Fig. 1. Droplet trajectories for Case 40.

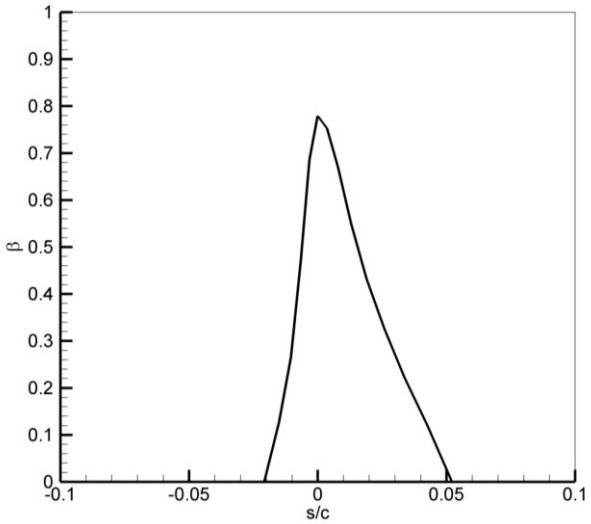

Fig.2. Collection efficiency distribution for Case 40.

Convective Heat Transfer Coefficients

After flowfield and droplet trajectory calculations, boundary-layer and icing calculations are performed. The current study employs a 2-D Integral Boundary Layer Method for the calculation of the convective heat transfer coefficients for laminar and turbulent flow [1].

Extended Messinger Method

The ice prediction approach employed in this study is the same as the one used by Özgen and Canıbek [1,3]. The phase change problem is governed by energy equations in the ice and water layers, mass conservation equation and a phase change condition at the ice/water interface [4]:

$$\frac{\partial T}{\partial t} = \frac{k_i}{\rho_i C_{pi}}\frac{\partial^2 T}{\partial y^2}, \tag{7}$$

$$\frac{\partial \theta}{\partial t} = \frac{k_w}{\rho_w C_{pw}} \frac{\partial^2 \theta}{\partial y^2}, \tag{8}$$

$$\rho_i \frac{\partial B}{\partial t} + \rho_w \frac{\partial h}{\partial t} = \rho_a \beta V_\infty + \dot{m}_{in} - \dot{m}_{e,s}, \tag{9}$$

$$\rho_i L_F \frac{\partial B}{\partial t} = k_i \frac{\partial T}{\partial y} - k_w \frac{\partial \theta}{\partial y}, \tag{10}$$

where θ and T are the temperatures, k_w and k_i are the thermal conductivities, C_{pw} and C_{pi} are the specific heats and h and B are the thicknesses of water and ice layers, respectively. In equation (9), $\rho_a \beta V_\infty$, $\dot{m}_{in}$ and $\dot{m}_{e,s}$ are impinging, runback and evaporating (or sublimating) water mass flow rates for a control volume (panel), respectively. In equation (10), ρ_i and L_F denote the density of ice and the latent heat of solidification of water, respectively. The coordinate y is normal to the surface. In order to determine the ice, water thicknesses and the temperature distribution at each layer, boundary and initial conditions must be specified. These are based on the following assumptions [4]:

1. Ice is in perfect contact with the wing or duct surface, which is taken to be equal to the recovery temperature:

$$T(0,t) = T_s. \tag{11}$$

$$T_s = T_a + \frac{V_\infty^2 - U_e^2}{2C_p} \frac{1 + 0.2rM^2}{1 + 0.2M^2}. \tag{12}$$

2. The temperature is continuous at the ice/water boundary and is equal to the freezing temperature:

$$T(B,t) = \theta(B,t) = T_f. \tag{13}$$

3. At air/water (glaze ice) or air/ice (rime ice) interfaces, heat flux is governed by convection (Q_c), radiation (Q_r), latent heat release (Q_l), cooling by incoming droplets (Q_d), heat brought by runback water (Q_{in}), evaporation (Q_e) or sublimation (Q_s), aerodynamic heating (Q_a) and kinetic energy of incoming droplets (Q_k).

   Glaze ice:

$$-k_w \frac{\partial \theta}{\partial y} = (Q_c + Q_e + Q_d + Q_r) - (Q_a + Q_k + Q_{in}) \quad \text{at} \quad y = B + h. \tag{14}$$

   Rime ice:

$$-k_i \frac{\partial T}{\partial y} = (Q_c + Q_s + Q_d + Q_r) - (Q_a + Q_k + Q_{in} + Q_l) \quad \text{at} \quad y = B. \tag{15}$$

4. Wing surface is initially clean:

$$B = h = 0, \quad t = 0. \tag{16}$$

The expressions for the heat terms can be found in [1].

Rime Ice Growth and Temperature Distribution:

In the current method, each panel constituting the airfoil is also a control volume. The above equations are solved for each panel and ice accumulates perpendicularly to a panel.

Rime ice thickness is obtained directly from the mass conservation equation (9) as water droplets freeze immediately on impact:

$$B(t) = \frac{\rho_a \beta V_\infty + \dot{m}_{in} - \dot{m}_s}{\rho_r} t. \tag{17}$$

For ice thicknesses less than 2.4 cm (which the case for most applications), the temperature distribution is governed by [4]:

$$\frac{\partial^2 T}{\partial y^2} = 0. \tag{18}$$

Integrating the above equation twice and applying the boundary and interface conditions given in equations (11) and (13) results in the following temperature distribution in the rime ice layer:

$$T(y) = T_s + \frac{(Q_a + Q_k + Q_{in} + Q_l) - (Q_c + Q_d + Q_s + Q_r)}{k_i} y. \tag{19}$$

Glaze Ice Growth and Temperature Distribution:

If ice and water layer thicknesses are less than 2.4 cm and 3 mm (true for most applications), respectively, the temperature distributions in the ice and water layers are governed by the following equations [4]:

$$\frac{\partial^2 T}{\partial y^2} = 0, \quad \frac{\partial^2 \theta}{\partial y^2} = 0. \tag{20}$$

After integrating above equation twice and employing the conditions (11) and (13), the temperature distribution in the ice:

$$T(y) = \frac{T_f - T_s}{B} y + T_s. \tag{21}$$

The temperature distribution in the water layer is obtained by integrating equation (20) twice and employing the interface conditions (13) and (14):

$$\theta(y) = T_f + \frac{(Q_a + Q_k + Q_{in}) - (Q_c + Q_d + Q_e + Q_r)}{k_w} (y - B). \tag{22}$$

Integrating mass conservation equation (9) yields the water height, h:

$$h = \frac{\rho_a \beta V_\infty + \dot{m}_{in} - \dot{m}_e}{\rho_w} (t - t_g) - \frac{\rho_g}{\rho_w} (B - B_g), \tag{23}$$

where B_g is the rime ice thickness at which glaze ice first appears and t_g is the time at which this happens. When equation (23) is substituted into the phase change condition in equation (10), a first order ordinary differential equation for the ice thickness is obtained:

$$\rho_g L_F \frac{\partial B}{\partial t} = \frac{k_i (T_f - T_s)}{B} + k_w \frac{(Q_c + Q_e + Q_d + Q_r) - (Q_a + Q_k + Q_{in})}{k_w}. \tag{24}$$

In order to calculate the glaze ice thickness as a function of time, equation (24) is integrated numerically, using a Runge-Kutta-Fehlberg method [5].

RESULTS AND DISCUSSION

The developed code has been run for three different test cases ranging from incompressible to highly compressible flow conditions taken from reference [2]. The flow and cloud properties for these cases are presented in Table 1. The geometry is the SA 13112 airfoil with a chord length of 0.6 m, and the median volumetric diameter of the droplets is 20 microns.

Table 1. Flow and cloud properties for the studied cases.

Variable	Case 40	Case 41	Case 42
α (°)	10	0	0
V_∞ (m/s)	81.3	162.5	249.9
M	0.25	0.50	0.80
T_a (°C)	-10	-10	-30
ρ_a (kg/m^3)	0.5	0.5	0.5
t_{exp} (s)	900	450	180

Figure 3 shows the results and comparisons with experimental and numerical data for Case 40 reported in the literature [2]. According to the numerical results, the ice mainly collects over the lower surface of the airfoil due to high angle of attack, although the agreement with the reported experimental ice shape is poor. However, the current results agree well with the numerical results reported in the literature, especially with those obtained by NASA and ONERA. There is very good match in the way iced region has been predicted. Another noteworthy inference is that due to low Mach number, there is very little difference in the results when compressibility effects are switched on and off in the developed computational tool.

Figure 4 depicts the results of Case 41, where the flow is compressible, as M=0.5. Neither the current results nor other numerical results reported agree well with the experimental ice shape but the agreement of the current results with those of NASA and ONERA is remarkable both in terms of the ice shape and the extent of the iced region.

An interesting outcome is that, in the computed ice shape there is a clean region in the vicinity of the leading edge although this region clearly remains within the impingement zone of the droplets. However, aerodynamic heating, which is prominent for high speed flows increases the surface temperature in this zone above the freezing temperature preventing any ice formation there. The unfrozen water behaves as runback water on the upper and lower surface of the airfoil, eventually resulting in the two prominent horns immediately downstream of the leading edge.

As can also be seen in the same figure, when high speed flow effects are included in the analysis, the ice mass becomes less compared to similar conditions in the low-speed range. Comparing the ice shapes predicted by switching the compressibility effects on and off, it is observed that the ice shape predicted by switching compressibility effects off result in a smoother ice shape with greater volume. When compressibility effects are switched on, due to higher amount of runback water, one obtains more irregular ice shapes as shown in the figure. The lift and drag characteristics of most airfoils are strongly dependent on the nature of the flow just downstream of the leading edge on the upper surface. Therefore, perturbed flow in this region is likely to result in a more severe degradation in the aerodynamic performance of the airfoil. As a result, inclusion of high speed effects allows more realistic conclusions to be reached in terms of aerodynamic performance.

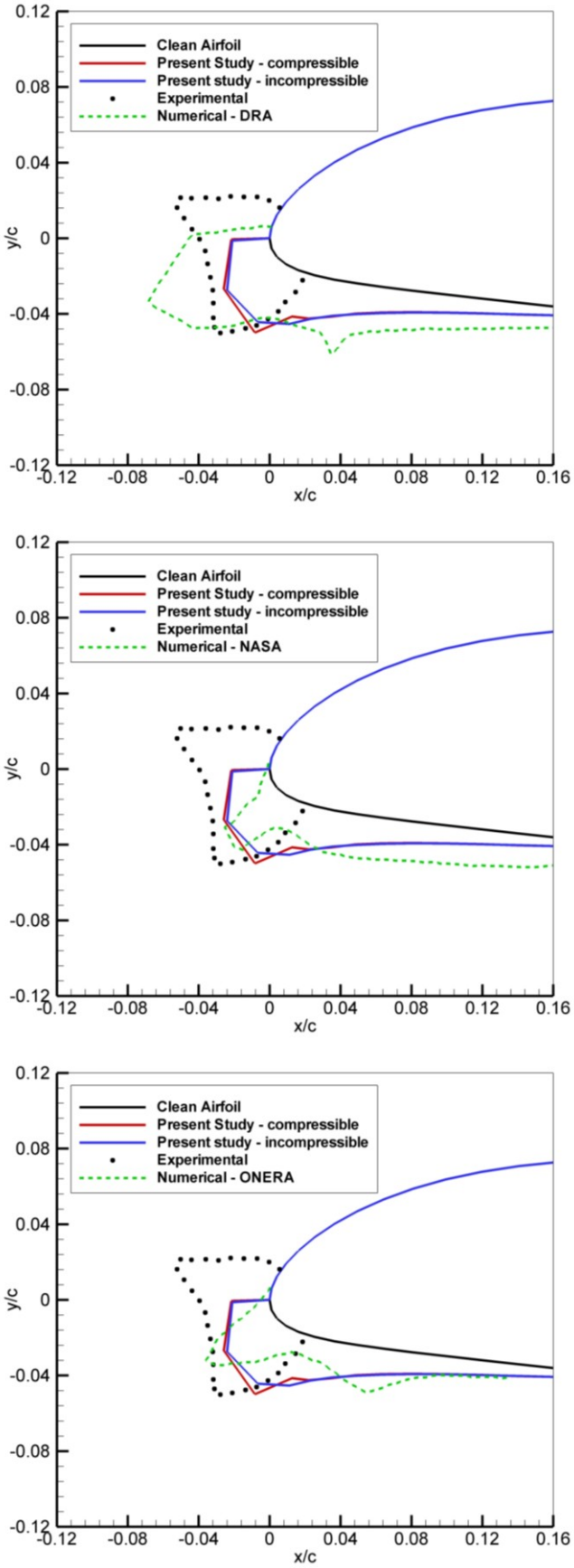

Fig. 3. Ice shapes for Case 40 (M=0.25).

Finally, Figure 5 illustrates the results of a highly compressible case, Case 42, corresponding to M=0.8. For this case, there is no experimental data available so the comparison of the current results will be done against numerical results only. This Mach number is at the limit of the validity of the Prandtl-Glauert compressibility correction rule. In this figure, the difference of the results when compressibility is accounted for or not is more clear. When compressibility effects are not accounted for, the results exhibit a typical rime ice shape with smooth contours. The ice formation is almost fully rime because of the low ambient temperature and low LWC. However, when compressibility is accounted for, we see that the ice shape is much more irregular, hinting that at least some glaze ice formation is present. This is expected because the local temperatures at the airfoil surface are effectively much higher than the ambient temperature due to aerodynamic heating. There is even a very narrow region with no ice formation suggesting that the surface temperature there is above the freezing temperature.

Unfortunately, the current results do not agree well with both experimental and numerical results. However, the agreement of the predicted ice extent agrees remarkably well with that of DRA. The reason for the discrepancy may be that compressibility is not directly accounted for in the boundary-layer calculations for computing the convective heat transfer coefficients and in the Extended Messinger Method.

CONCLUSIONS AND FUTURE WORK

The presented computational tool has been undergoing continuous development since it was first programmed in 2007. The current features include treatment of supercooled large droplets (SLD) and non-spherical cloud droplets by taking droplet breakup and splash into account. As outlined in this study, compressibility effects are partially accounted for and the results seem encouraging.

A three-dimensional version of the code using almost the same strategy and methodology has also been developed, which has similar features. Since droplet trajectory calculations consume a lot of CPU, in the 3-D tool, this task has been parallelized. Upon parallelization, an almost linear speed-up and high efficiency has been obtained [6, 7].

Further work prospects include implementation of Euler methods both for the flowfield and the droplet trajectory computations since this will allow more complex geometries to be treated and allow local variations in the LWC, as this has been shown to be prominent. The same upgrade will allow treatment of a flowfield with non-uniform temperature, which is an important aspect of trajectory and icing calculations in turbofan engines. Another improvement may be to develop and implement a module that can handle ice crystals as well as liquid droplets.

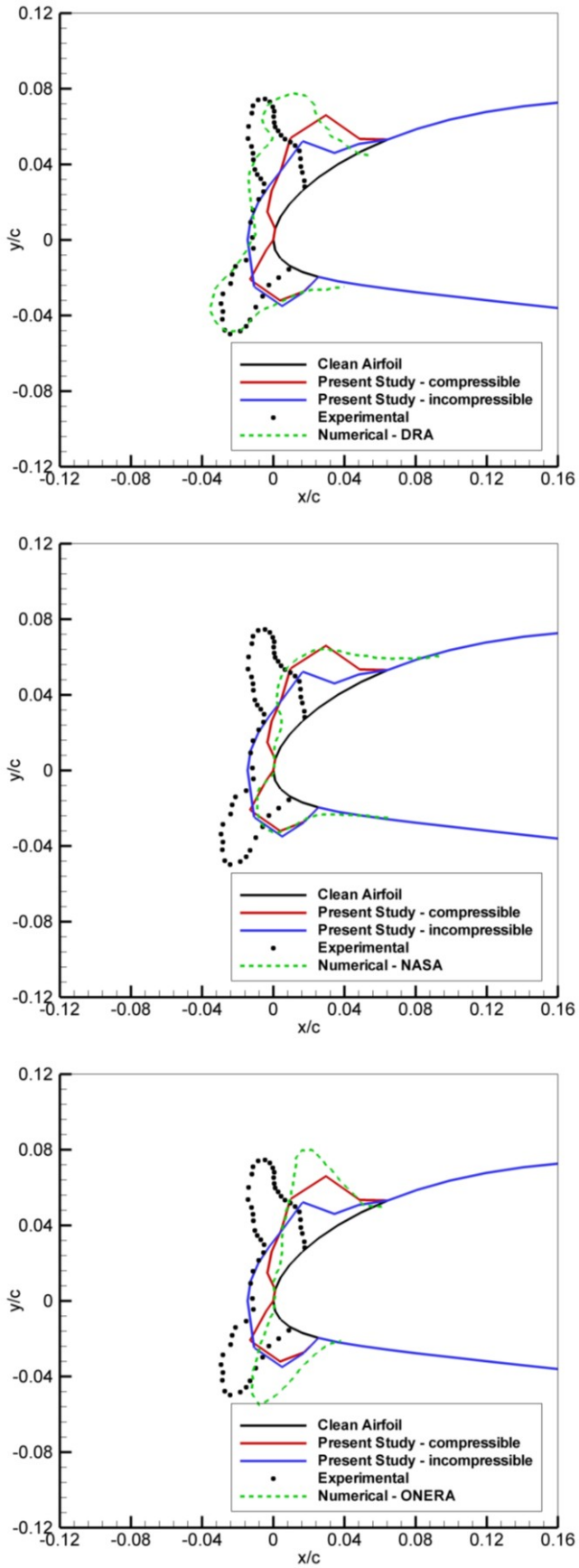

Fig. 4. Ice shapes for Case 41 (M=0.50).

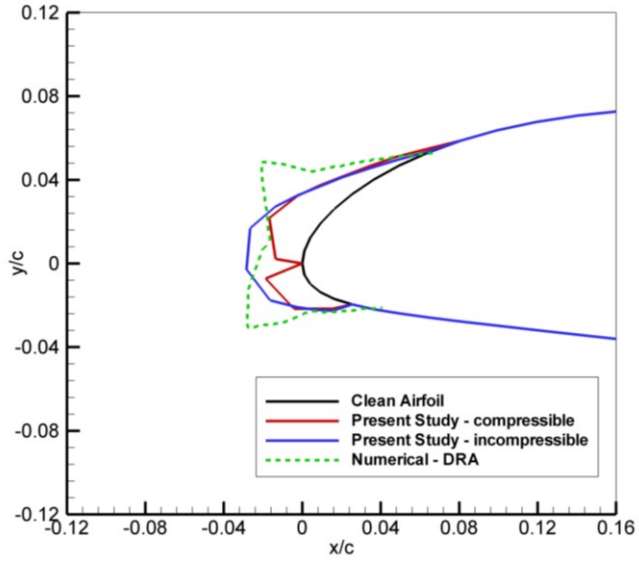

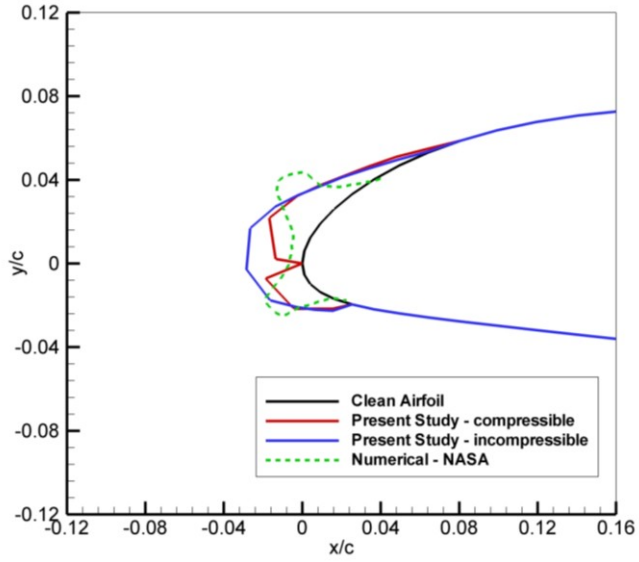

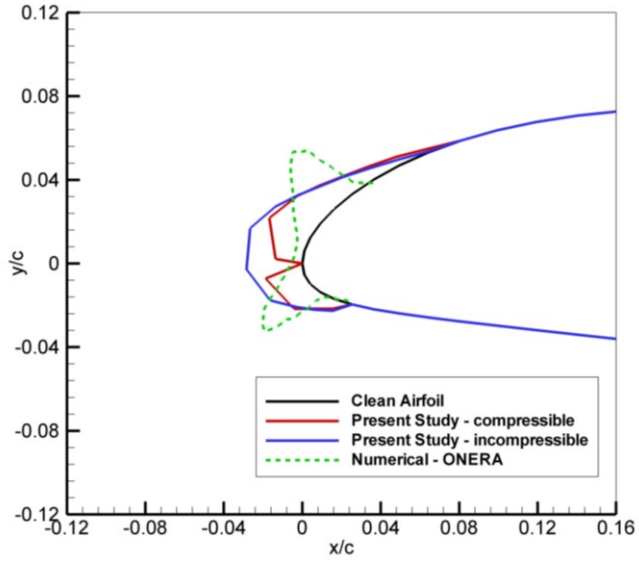

Fig. 5. Ice shapes for Case 42 (M=0.80).

REFERENCES

[1] Özgen, S., and Canıbek, M., Ice Accretion Simulation on Multi-Element Airfoils using Extended Messinger Model, *Heat and Mass Transfer*, Vol. 45, 2009, pp. 305-322.

[2] Wright, W., Gent, R., and Guffond, D., DRA/NASA/ONERA Collaboration on Icing Research, Part II, Prediction of Airfoil Ice Accretion, NASA CR_202349, 1997.

[3] Özgen, S. and Canıbek, M., In-Flight Icing Simulation with Supercooled Large Droplet Effects, *Proceedings of the 7th International Conference on Heat Transfer, Fluid Mechanics and Thermodynamics (HEFAT'2010), Antalya, Turkey,* 2010.

[4] Myers, T.G., Extension to the Messinger Model for Aircraft Icing, *AIAA J.*, Vol. 39, 2001, p.211-218.

[5] Mathews, J. H., Numerical Methods, Prentice-Hall, London, 1987, p. 423-432.

[6] Özgen, S., Tarhan, E., Canıbek, M., Parallel Computing Applied to Three-Dimensional Droplet Trajectory Simulation in Lagrangian Approach, SAE Paper 2011-38-106, 2011.

[7] Özgen, S., Tarhan, E., Canıbek, M., 3-D In-Flight Icing Simulations and Use of Parallel Computing in Lagrangian Droplet Trajectory Calculations, *Proceedings of the 6. Ankara International Aerospace Conference (AIAC'2011), Ankara, Turkey,* 2011.